Discerning the mechanism of expedited interfacial electron transformation boosting photocatalytic hydrogen evolution by metallic 1T-WS$_2$-induced photothermal effect

Yuan Tang [a], Wei Zhou [d], Qianqian Shang [c], Yuchen Guo [a], Huilin Hu [e], Zhiqiang Li [a], Yizhong Zhang [a], Lequan Liu [e], Huaiyuan Wang [b], Xin Tan [a,f], Tao Yu [b,*], Jinhua Ye [e,g]

[a] School of Environmental Science and Engineering, Tianjin University, No. 135 Yaguan Road, Jinnan District, Tianjin 300350, China
[b] School of Chemical Engineering and Technology, Tianjin University, No. 135 Yaguan Road, Jinnan District, Tianjin 300350, China
[c] College of Chemistry and Chemical Engineering, Liaocheng University, No.1, Huanan Road, Liaocheng 252000, China
[d] School of Science, Tianjin University, No. 135 Yaguan Road, Jinnan District, Tianjin 300350, China
[e] TJU-NIMS International Collaboration Laboratory, Tianjin University, No. 92 Weijin Road, Nankai District, Tianjin 300072, China
[f] School of Science, Tibet University, No. 36 Jiangsu Road, Lhasa 850000, China
[g] International Center for Materials Nano Architectonics (WPI-MANA), National Institute for Materials Science (NIMS), 1-1 Namiki, Tsukuba 305-0047, Japan

ARTICLE INFO

ABSTRACT

Modulation of electronic structure and facilitation of *H adsorption through defective sites is of great significance for photocatalytic hydrogen evolution. Here, we designed an S vacancies 1T-WS$_2$/CdS to achieve 70.9 mmol/g/h hydrogen evolution rate accompanied with 39.1% AQY at 500 nm via coordinating the interfacial electronic engineering and photothermal effect. The photothermal effect induced by S vacancies 1T-WS$_2$ effectively lowered the apparent activation energy from 15.96 kJ/mol to 10.51 kJ/mol, meanwhile, the directional migration of electrons from CdS to S vacancies accelerated by lattice heating was the main reason for boosting photocatalytic hydrogen evolution. Both the decrease of free energy of *H due to the existence of S vacancies and the enhancement of field strength caused by effective enrichment of electrons at the interface of S vacancies 1T-WS$_2$/ CdS. This work provided valuable insight into the use of non-precious metal co-catalysts for photo-thermal assisted photocatalytic hydrogen evolution.

1. Introduction

As a clean and renewable energy source, hydrogen is considered as an emerging supplementary energy source that can replace the fossil fuel with the deterioration of the environment and the depletion of fossil fuel [1,2]. With the development of hydrogen production technology, photocatalytic hydrogen evolution was thought as the most promising technology for hydrogen energy development, although it was still limited by the solar energy utilization and efficient charge separation capability of photocatalysts [3,4]. Recently, a large amount of research on defect engineering have emerged, and it was found that defect engineering had a significant impact both on the regulation of interface electronic structure and active sites. Recently, co-catalysts have been extensively investigated to create surface active sites to facilitate the separation of photogenerated carriers. Yu et al. designed a core-shell

Au@NiS$_{1+x}$ co-catalyst to modify TiO$_2$, where photogenerated electrons were induced to transfer from Au to NiS$_{1+x}$, and the resulting electron-rich S$^{\delta-}$ active sites weakened the S-Hads bond and facilitated the desorption of H$_{ads}$ to generate hydrogen [5]. As we all know, defects in the photocatalyst can both serve as traps for photogenerated electrons to promote the separation of photogenerated carriers and act as the recombination center of photogenerated carriers reduced the photocatalytic activity [6,7]. Conclusively, how to design and fabricate the controllable the defect site on the co-catalyst to accelerate the photoreduction process is the prerequisite to ensure optimal photoactivity [8].

As a representative anionic defect, many studies have reported that S vacancies can provide sufficient adsorption and active sites for carriers and increase the light absorption range of catalysts through defect energy levels [9]. The appropriate vacancy concentration can enhance the electron capture ability of the co-catalyst to facilitate surface charge

separation and transfer [10]. Although the S vacancies-modified co-catalysts have exhibited excellent photocatalytic hydrogen evolution performance, the limited rate of charge migration at the interface has still prevented their further application. That gives a significant advantage to the photothermal effect induced by noble metal co-catalysts in the introduction of photocatalytic hydrogen evolution [11,12]. However, the utilization of precious metals is greatly reduced due to their scarcity and high price, as well as their poor chemical stability [13–15].

1T-phase transition metal sulfides (TMDs) are widely used as co-catalysts in photocatalysis and thermal catalysis due to their ultra-high electrical conductivity and abundant substrate active sites that are superior to 2H-phase TMDs [16–19]. Liang et al. [20]. used metal 1T-WS$_2$ as a co-catalyst to combine with g-C$_3$N$_4$ obtained an improved photocatalytic hydrogen evolution efficiency (1021 μmol/h/g). Stanley S. Chou et al. [21]. first demonstrated that metal 1T-MoS$_2$ could serve as excellent photothermal agents. Recently, researchers have explored defective 1T-WS$_2$ in the field of electrocatalysis in depth [22]. Cui et al. [23]. used S vacancies defect excitation to modulate the inert substrate surface of 1T-WS$_2$ for electrocatalytic hydrogen evolution. However, studies on the application of S vacancies 1T-WS$_2$ as a co-catalyst for photocatalytic hydrogen evolution are relatively lacking. Here we considered the potential of metal 1T-WS$_2$ to promote charge migration kinetics acceleration by photothermal effect [18]. Therefore, the S vacancies 1T-WS$_2$ was used as a co-catalyst to provide a platform for efficient carrier trapping and *H adsorption. To our knowledge, there is a lack of studies on the photothermal effect induced by 1T-phase transition metal sulfides (TMDs), and the mechanism of its photothermal effect in the liquid-phase reaction environment needs to be further revealed.

In this study, a S vacancies 1T-WS$_2$ (Vs-1T-WS$_2$) was used as a photothermal cocatalyst and compounded with CdS to enhance the photocatalytic hydrogen evolution. The optimized Vs-1T-WS$_2$/CdS (Vs-1T-WCS) complex could achieve a hydrogen evolution performance of 70.9 mmol/g/h at 500 nm with an apparent quantum yield (AQY) of 39.1%. The introduction of Vs-1T-WS$_2$ not only expanded the photoreaction range, but also promoted the reaction kinetics and accelerated the directional migration of electrons from CdS to S vacancies through the induced photothermal effect. More importantly, as the reaction and adsorption sites, the S vacancies modulated the interfacial electronic structure to promote photocatalytic hydrogen evolution.

2. Experimental section

2.1. Synthesis of Vs-1T- WS$_2$

397 mg WCl$_6$ and 750 mg CH$_3$CSNH$_2$ were added into 30 mL DMF and stirred for 1 h. The above mixed solution was ultrasonicated in an ultrasonic cleaner for 1 h and then transferred to a 50 mL Teflon autoclave and heated at a constant temperature of 200 °C for 24 h. After the reactor was cooled to room temperature naturally, the black precipitation products were washed with distilled water and anhydrous ethanol three times by centrifugation; the black powder was dried at 60 °C for 12H. The resulting black powder was 1T-phase WS$_2$ nanosheets, which was recorded as Vs-1T-WS$_2$.

2.2. Synthesis of Vs-1T-WCS

Different masses of Vs-1T-WS$_2$ (14 mg, 43 mg, 60 mg) were added to 30 mL distilled water and dispersed and sonicated for 1 h. To the above suspensions, 533 mg Cd (CH$_3$COOH)$_2$·2H$_2$O and 300 mg CH$_3$CSNH$_2$ were added and stirred for 1 h. The above mixture was transferred to a 50 mL Teflon autoclave and heated at 180 °C for 24 h. The precipitated product was obtained by centrifugation and washed three times with distilled water and anhydrous ethanol in turn. The obtained products of Vs-1T-WS$_2$ were noted as Vs-1T$_{0.05}$-WCS, Vs-1T$_{0.15}$-WCS, Vs-1T$_{0.25}$-

WCS, depending on the mass fraction of Vs-1T-WS$_2$.

2.3. Materials characterization

The physical phase structures of Vs-1T-WS$_2$, CdS and Vs-1T-WCS were analyzed by X-ray diffractometry (XRD, Bruker D8-Focus, Germany) and Raman spectroscopy (excitation wavelength 532 nm, XPLORA plus, France). The microscopic morphology and lattice structure of the prepared samples were obtained by S-4800 field emission scanning electron microscopy (SEM, Japan) and FEI Tecnai G2 F20 transmission electron microscopy (TEM, The Netherlands) with its accompanying high-angle annular dark field (HAADF) and energy dispersive X-ray spectroscopy (EDS) images. The chemical state of the prepared samples was characterized by Thermo Scientific X-ray photoelectron spectroscopy (XPS, Al Kα source, USA). The optical properties of the prepared materials were evaluated by obtaining UV–vis diffuse reflectance spectra (UV–vis DRS) using a UV-3600 UV–vis spectrophotometer (excitation wavelength of 365 nm, Japan). Photoluminescence (PL) spectral measurements for analyzing the photogenerated electron-hole complexation rate of the materials were performed on a Fluorolog-3 fluorescence spectrophotometer (excitation wavelength of 330 nm, Hitachi, Japan). Time-resolved photoluminescence (TRPL) spectra were recorded on a FLS1000 fluorescence lifetime spectrophotometer (UK). Surface photovoltage (SPV) measurements in the light and dark were measured by a Kelvin probe force microscope (KPFM) configured with a 300 W Xe lamp source. Prior to testing, the probe was calibrated with an iron sheet and the test sample was uniformly dispersed on the iron conductive sheet. The surface temperature of the catalyst is measured by the Testo 865 thermal imaging camera (China). It is measured by spreading 0.1 g of catalyst on white paper and irradiating it with visible light (λ ≥ 420 nm) for 1 min. The electron spin resonance spectra (ESR) were obtained electronically using a JES-FA200 (Japan) spectrometer for detecting the presence of S vacancies and photogenerated electrons, where the photogenerated electrons were obtained by TEMPO (2,2,6,6-tetramethylpiperidine nitrogen oxide) capture.

2.4. Photocatalytic H$_2$ evolution

The photocatalytic hydrogen evolution experiments were performed in a 350 mL closed reaction tank. The photocatalytic hydrogen precipitation performance was tested in the full spectral range of visible light (λ ≥ 420, 500, 600) and AM1.5 by using a 300 W xenon lamp as a light source. A 300 W xenon arc lamp with UV cut-off filter (≥ 420 nm) was used as a visible light source to activate the photocatalytic reaction. In a typical photocatalytic reaction, 20 mg of photocatalyst was dispersed in 30 mL of aqueous lactic acid (10 vol%) solution. The temperature of the reaction system is continuously controlled by a cooling circulating water system at 10 °C. The reaction gas line was evacuated to remove excess gas from the system prior to photoluminescence, and the product was exported from the reaction tank at each hour of the reaction and analyzed for H$_2$ concentration by an on-line GC-14C gas chromatograph (Shimadzu, Japan) with a thermal conductivity detector (TCD).

Apparent quantum yield (AQY) measurements were performed using a 300 W xenon lamp as the light source. Monochromatic light was obtained by filtering through band-pass filters of different wavelengths. AQY was calculated according to the following equation:

$$AQY = \frac{number \quad of \quad photons \quad utilized \quad in \quad H_2 \quad evolution}{total \quad number \quad of \quad photons} = \frac{2R_{H_2}N_A}{n}$$

(1)

$(R_{H_2} = H_2 \quad production \quad rate, \quad N_A = Avogadro \quad constant)$

Experiments on the activation energy of photocatalytic hydrogen evolution at different temperatures: the reaction temperature was controlled by condensing water at 4, 8, 12 and 16 °C to measure the rate of photocatalytic hydrogen evolution at different temperatures. Here,
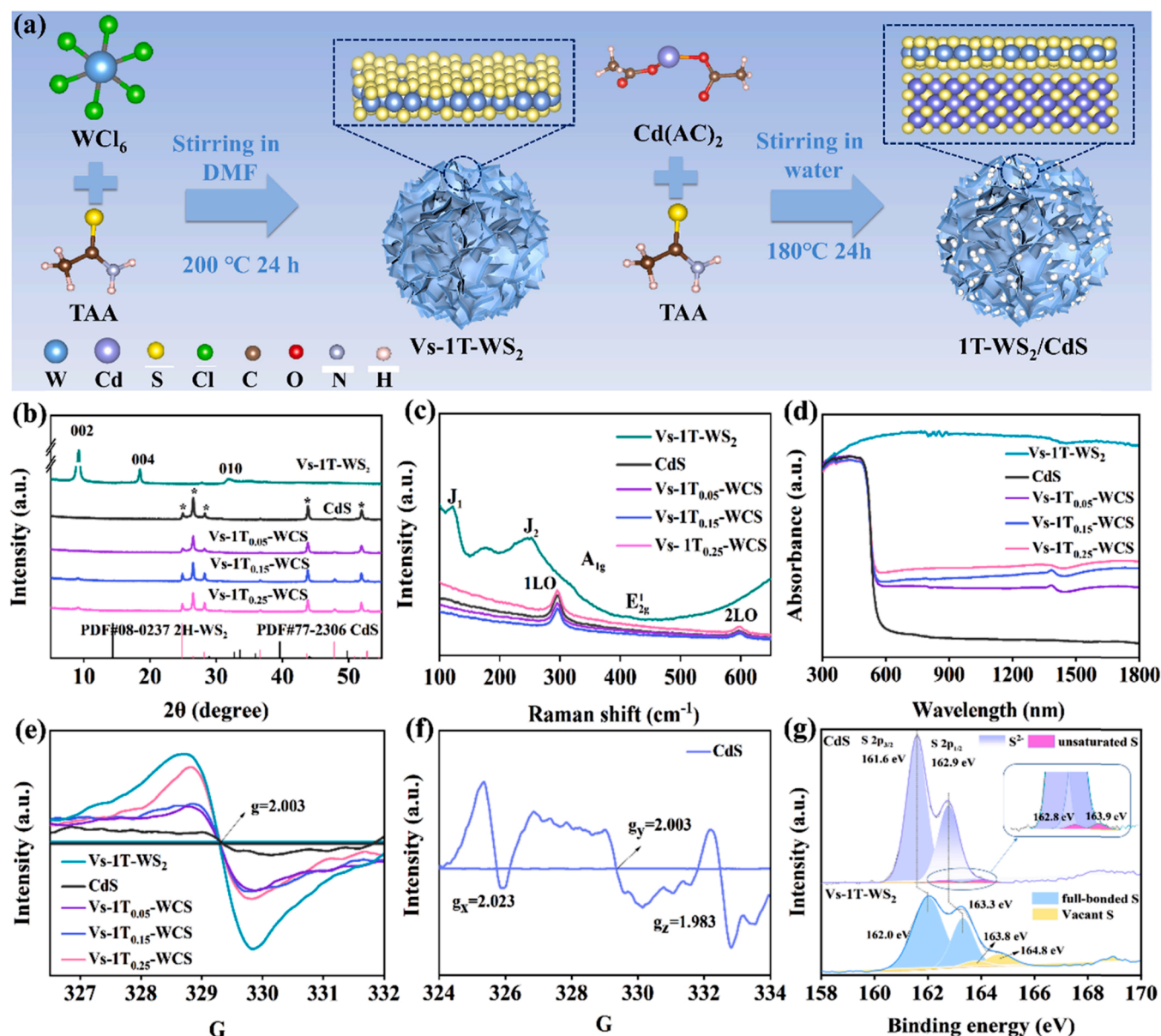
Fig. 1. Structural characterization of the prepared catalysts. (a) Schematic diagram of the synthesis route of Vs-1T-WCS, (b) XRD spectrum, (c) Raman spectrum, (d) UV–vis-NIR diffuse reflectance spectroscopy and (e) electron paramagnetic resonance (EPR) spectra of Vs-1T-WS$_2$, CdS, and Vs-1T-WCS, (f) EPR spectra of CdS, (g) S 2p XPS spectra of Vs-1T-WS$_2$ and CdS.

the apparent activation energy (*Ea*) of photocatalytic hydrogen precipitation of the prepared samples was calculated according to the Arrhenius equation as follows:

$$lnk = -\frac{E_a}{RT} + lnA \tag{2}$$

where *A* was the frequency factor, *T* was the thermodynamic temperature of the reaction, *Ea* was the apparent activation energy, *k* was the reaction rate constant, and *R* was the molar gas constant.

3. Results and discussion

3.1. Characterization of Vs-1T-WS$_2$, CdS and 1T-WCS

CdS nanoparticles were in situ fixed on the surface of Vs-1T-WS$_2$ nanoflowers to fabricate the desired Vs-1T-WCS composites via a solvothermal method (Fig. 1a). The phase compositions and crystal structures of CdS, Vs-1T-WS$_2$, 2H-WS$_2$, and Vs-1T-WCS were analyzed by XRD and Raman spectroscopy (Fig. 1b). The major sharp peaks of CdS matched well with the typical hexagonal phase of CdS (PDF 77–2306) [24,25], and the typical peaks at 9.4°, 18° and 32° in Vs-1T-WS$_2$ were assigned to the (002), (004) and (010) crystal planes, respectively. Notably, the position of (002) crystal plane in Vs-1T-WS$_2$ was shifted from 9.4° to 14.4° compared to 2H-WS$_2$ (PDF 08-0237), which was attributed to the phase transformation due to the increased layer spacing (Fig. S1) [26,27]. The peaks located at 125 cm^{-1} and 255 cm^{-1} stemmed from J1 and J2 modes in Vs-1T-WS$_2$ detected by Raman spectra (Fig. 1c) [28,29], and the distinct vibrational peaks of CdS located at 299 cm^{-1} and 598 cm^{-1} were classified to 1LO and 2LO optical phonon modes of CdS, respectively [30,31]. No vibration peaks other than CdS in Vs-1T-WCS was caused by the low loading of Vs-1T-WS$_2$. UV-Vis-NIR diffuse reflectance spectra demonstrated no fixed absorption edge in Vs-1T-WS$_2$ with a wide wavelength range of 300–1200 nm absorbance, which implied that Vs-1T-WS$_2$ could replace noble metals to induce photothermal effects and achieved a wider solar spectrum absorption.
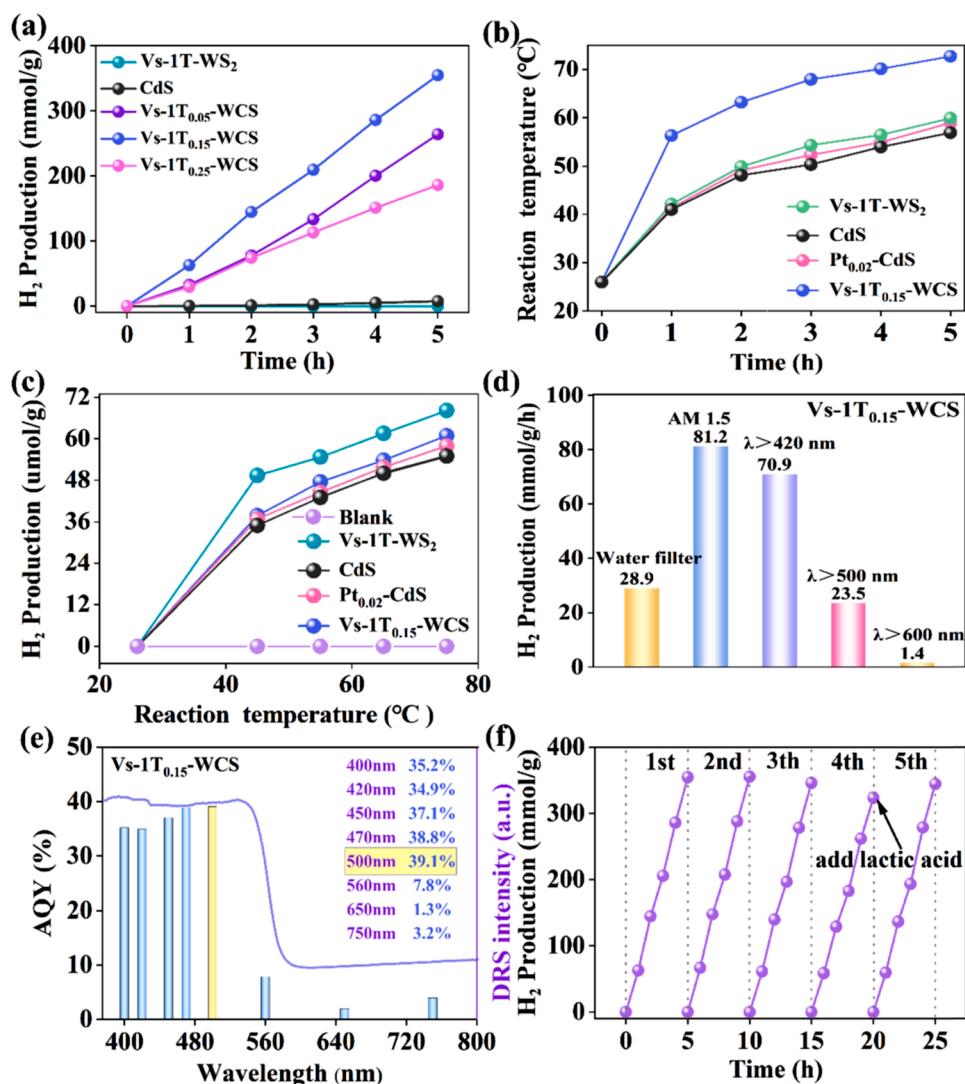
Fig. 2. Photocatalytic H₂ evolution performance. (a) H₂ evolution amount of Vs-1T-WS₂, CdS and Vs-1T-WCS at different irradiation time, (b) reaction temperatures of photocatalytic hydrogen precipitation reaction systems with different catalysts, (c) thermal catalytic hydrogen evolution performance of the prepared samples at different temperatures, (d) photocatalytic hydrogen evolution performance of Vs-1T$_{0.15}$-WCS under different wavelengths of light irradiation, (e) the wavelength-dependent apparent quantum yield of Vs-1T$_{0.15}$-WCS, (f) photocatalytic hydrogen evolution stability experiment of Vs-1T$_{0.15}$-WCS.

Compared to pristine CdS, both redshift absorption edge and increased absorption intensity from 550 nm to the near-infrared region were observed in Vs-1T-WCS. The energy band structures of the samples were determined based on the Mott-Schoktty curves and the band gap energies (Fig. S2). The morphological structures of Vs-1T-WS₂, 2H-WS₂, CdS and Vs-1T-WCS were scanned by SEM (Fig. S3) and TEM. CdS nanoparticles were well dispersed on the surface of Vs-1T-WS₂ nanoflower in Vs-1T-WCS, compared to dispersed in thick 2H-WS₂ nanosheets (Fig. S4) The EDS spectra and elemental mapping of Vs-1T-WCS demonstrated that the S, Cd and W elements were uniformly distributed on the surface (Fig. S5). The characteristics of unpaired electrons with low spin levels in S 3p orbit was clarified to expound the contribution of S vacancies for photocatalytic hydrogen evolution. The increased S vacancies (g=2.003) concentration in Vs-1T-WCS was accompanied with the increase of Vs-1T-WS₂ content (Fig. 1e) [32], which implied that the Vs-1T-WS₂ co-catalyst acted as an electron collector to facilitate the transfer of photogenerated carriers due to the unpaired electrons in the S 3p orbitals [33]. Besides, broad signal peaks with $g_x = 2.023$ and $g_z = 1.983$ were detected in CdS (Fig. 1f) [34], which were ascribed to unsaturated S atoms on CdS surface induced by deep energy levels [35]. We found that the photocatalytic hydrogen evolution rate was not exactly proportional to the concentration of S vacancies. A suitable vacancy concentration could promote the directional migration of photogenerated carriers to facilitate photocatalytic

hydrogen evolution. More importantly, both the unsaturated S sites of CdS and the S vacancies on Vs-1T-WS₂ had the potential to serve as *H adsorption sites [36], and the adsorption capacity for *H directly affected the performance of photocatalytic hydrogen evolution.

X-ray photoelectron spectroscopy (XPS) was performed to reveal the surface chemical composition of Vs-1T-WS₂, CdS and Vs-1T-WCS and the effect of S vacancies on the surface electronic properties. The actual atomic ratio of W/S was 1.00/1.24 in bare Vs-1T-WS₂, which provided a direct basis for the presence of S vacancies (Fig. S7). There were two different types of S 2p peaks in CdS (Fig. 1g), which were attributed to the basal plane S²⁻ and the unsaturated S site at the edge of CdS, respectively [34]. The peaks at 162.0 and 163.3 eV were attributed to the full-bonded S atoms in Vs-1T-WS₂ [37]. Meanwhile, the peaks at 162.8 and 163.9 eV with higher binding energy were attributed to the part-coordinated S atoms with higher valence states. The presence of these higher valence S atoms was attributed to the S vacancies in Vs-1T-WS₂ [38]. The W 4f spectrum of Vs-1T-WS₂ demonstrated the presence of three kind of W states (Fig. S8), in which the distinct peaks were assigned to the W 4f₇/₂ and W 4f₅/₂ of W(IV) in Vs-1T-WS₂ and 2H-WS₂, and W (VI) in WO₃ [39,40]. It was noted that the binding energies of W 4f and Cd 3d in Vs-1T-WCS were shifted in higher and lower directions compared to the pristine Vs-1T-WS₂ and CdS, respectively, as a result of interfacial interactions induced by the tight interfacial contacts of Vs-1T-WS₂ and CdS (Fig. S8) [41].
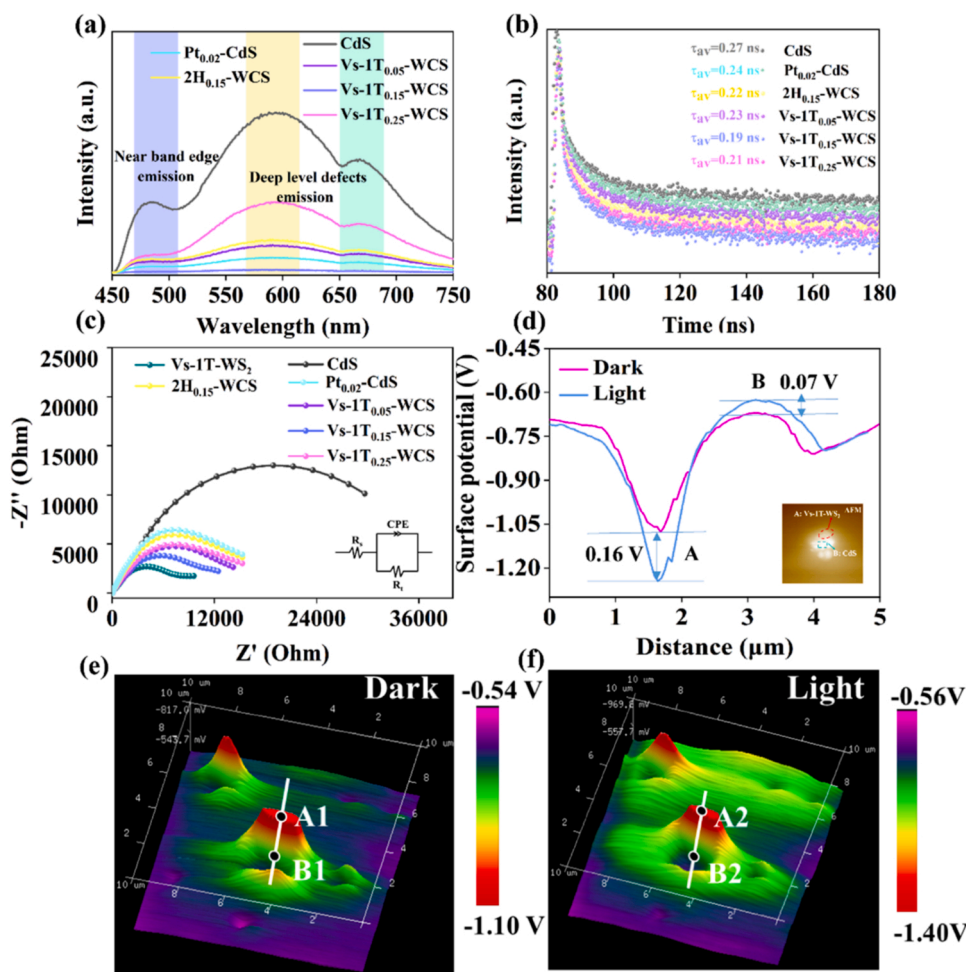
Fig. 3. Photophysical and electrochemical properties. (a) PL spectrum, (b) transient fluorescence emission spectra and (c) electrochemical impedance spectroscopy (EIS) of the as-prepared samples, (d) surface photovoltage under dark and visible light irradiation and AFM topography of Vs-1T$_{0.15}$-WCS, (e) surface photovoltage distribution of Vs-1T$_{0.15}$-WCS in the dark and (f) under visible light irradiation (KPFM).

3.2. Photocatalytic hydrogen evolution

In order to elaborate the priority performance of Vs-1T-WCS, the photocatalytic hydrogen evolution of Vs-1T-WCS, Pt-CdS and 2H-WCS was evaluated systematically here. The introduced metallic Vs-1T-WS$_2$ as cocatalyst significantly enhanced the photocatalytic hydrogen evolution rate to varying degrees, and the best performance was achieved at Vs-1T$_{0.15}$-WCS (70.93 mmol/g/h) (Fig. 2a). Both the optimized hydrogen evolution performance of Pt$_{0.02}$-CdS (20.2 mmol/g/h) and 2H$_{0.15}$-WCS (13.3 mmol/g/h) were significantly lower than that of Vs-1T$_{0.15}$-WCS (Fig. S9), which was attributed to the advantage of accelerated charge migration provided by the photothermal effect and the S vacancy in Vs-1T-WS$_2$. The photocatalytic hydrogen evolution rate was reduced greatly due to excessively loaded Vs-1T-WS$_2$ which shielded the incident light (Fig. S10a). Interestingly, Vs-1T$_{0.15}$-WCS still possessed excellent photocatalytic performance under different types of sacrificial agents, which indicated its broad application prospect (Fig. S10b). We noted that the temperature of the catalytic reaction system increased uniformly under visible light irradiation (Fig. 2b), which was due to the process of heat dissipation induced by the photothermal effect of Vs-1T-WS$_2$ leading to an increased temperature of the surrounding electrolyte. The thermal catalytic hydrogen evolution performance of all catalysts was enhanced with increasing reaction temperature in the dark (Fig. 2c). And the improved thermal catalytic hydrogen evolution of Vs-1T-WS$_2$ was observed compared to that of Vs-1T-WCS and CdS, which further demonstrated that Vs-1T-WS$_2$ acted as a thermal catalytic induced

lattice heating under temperature-driven. The hydrogen evolution performance of 2H-WS$_2$ and 2H$_{0.15}$-WCS at different temperatures was shown in Fig. S11, where the hydrogen evolution performance of 2H-WS$_2$ and 2H$_{0.15}$-WCS at different temperatures was significantly lower than that of Vs-1T-WS$_2$ and Vs-1T$_{0.15}$-WCS. The results indicated that 2H-WS$_2$ had no potential as a photothermal co-catalyst to induce photothermal effects, which further emphasized the advantages of Vs-1T-WS$_2$ as a metal co-catalyst for photocatalytic hydrogen evolution. We also obtained the same results by capturing the catalyst surface temperature with infrared thermography (Fig. S13) [42].

To illustrate the contribution of photothermal effects and inter band transition of charges at the interface for photocatalytic hydrogen evolution, various wavelength light was employed here to measure the photocatalytic performance of Vs-1T$_{0.15}$-WCS comprehensively. The best performance of 81.2 mmol/g/h was detected under simulated sunlight (AM 1.5), which was ascribed to the simultaneous excitation of the photothermal effect and inter-band transition of the charges at the interface (Fig. 2d). A significant reduction in photocatalytic hydrogen performance was observed under the incident light wavelength of λ > 500 nm (23.5 mmol/g/h), which was caused by the weakening of the inter band transition of charge with the diminished photon energy [43]. Due to the photothermal effect induced by metal Vs-1T-WS$_2$, the photocatalytic hydrogen evolution rate still achieved 1.4 mmol/g/h under the near infrared region light irradiation (λ > 600 nm). Compared with simulated sunlight, the photocatalytic performance of Vs-1T$_{0.15}$-WCS was reduced by 13.7% and 64.4% under λ > 420 nm
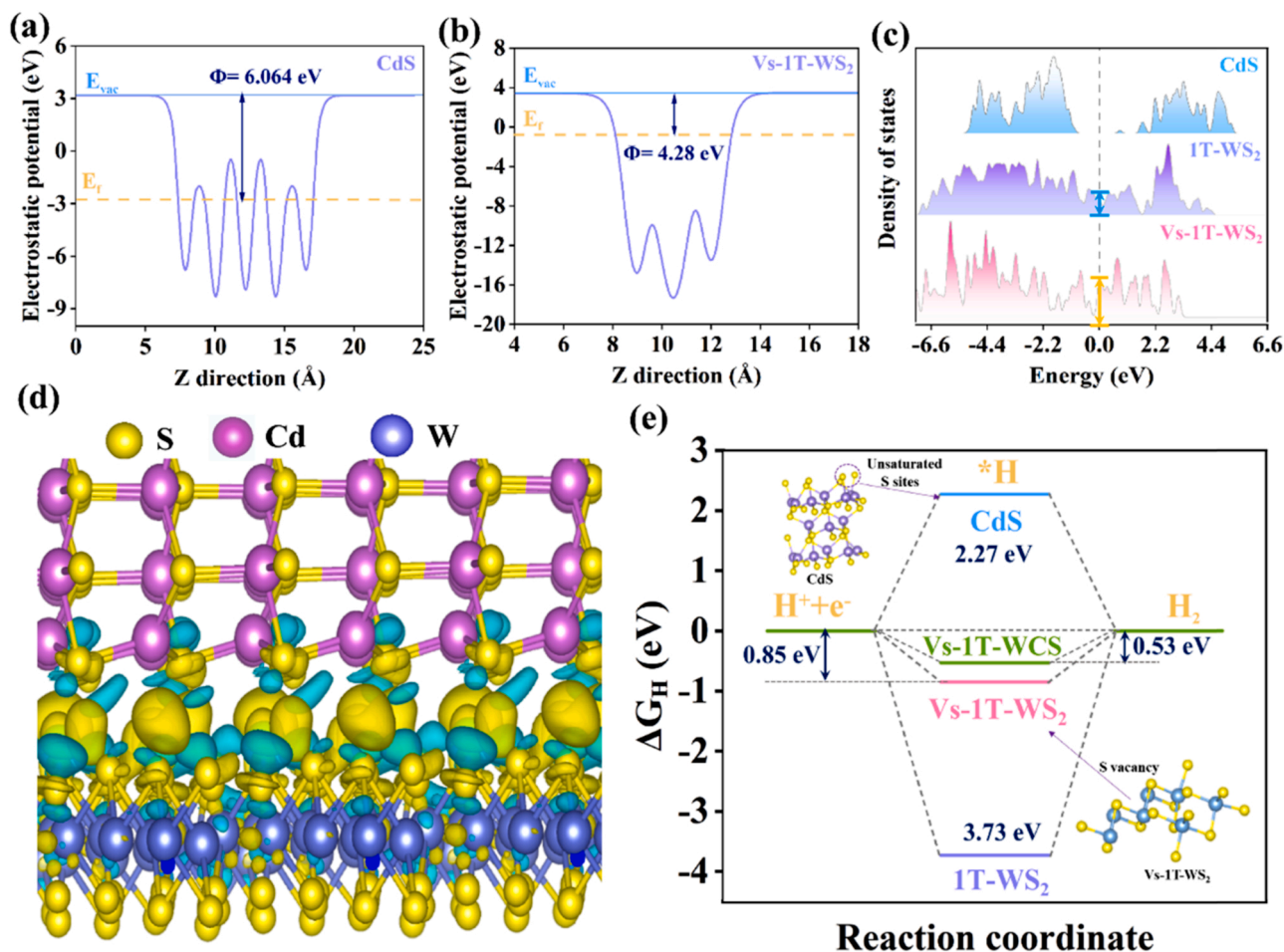
Fig. 4. Theory calculations. (a) The work functions of CdS and (b)Vs-1T-WS$_2$, (c) the total density states of CdS and Vs-1T-WS$_2$, (d) differential charge density of Vs-1T$_{0.15}$-WCS (cyan represented the electron enriched region and yellow represented the electron depleted region), (e)ΔG_H of the prepared catalysts (the calculated sites of CdS were at the edge of the unsaturated S atom and the calculated sites of Vs-1T-WS$_2$ were at the S vacancies site).

filter and water filter, respectively [44]. This result suggested that the photothermal effect originated from the thermal radiation generated by infrared light. Furthermore, the apparent quantum yield (AQY) of Vs-1T$_{0.15}$-WCS matched well with the UV-Vis absorption spectrum with an excellent AQY value of 39.1% at 500 nm, and there was an increasing trend of the photocatalytic hydrogen evolution rate detected in the near-infrared region (650–750 nm) (Fig. 2e). In summary, although the photothermal effect induced by Vs-1T-WS$_2$ activated the light absorption in the NIR region to accelerate the reaction kinetics, the directional migration of carriers at the interface caused by S vacancies was the main reason for improving the photocatalytic performance. Satisfactorily, there were almost no changes scanned in XRD, EIS, Raman (Fig. S14) and XPS spectra (Fig. S15) for Vs-1T$_{0.15}$-WCS before and after the reaction testified its excellent stability, which guaranteed the hydrogen evolution rate of Vs-1T$_{0.15}$-WCS maintained above 90% capacity after 25 h experiments (5 cycles) (Fig. 2f).

3.3. Photophysical and charge-transfer properties

Inter band transition of photogenerated carriers played a crucial role for the enhancement of photocatalytic performance, so the charge-transfer properties were further analyzed by electrochemical and photophysical characterization. There were three absorption bands with high intensity in CdS were determined by PL spectroscopy (Fig. 3a), where the absorption peak at 470 nm was attributed to the intrinsic near-band edge absorption of the photocatalyst and the remaining two peaks were classified to the extrinsic deep energy levels due to the

surface defect state [45]. The introduction of metal Vs-1T-WS$_2$ resulted in a significant decrease in the intensity of the PL peak of Vs-1T-WCS, which suggested that the S vacancies leaded to more intrinsic transfer of photogenerated electrons. At the same time, the average fluorescence lifetime (τ_{av}) of Vs-1T$_{0.15}$-WCS monitored a reduction trend with increasing Vs-1T-WS$_2$ content on the transient fluorescence emission spectra (Fig. 3b). This could be explained by the non-radiative interaction between the dipoles which caused more electrons transfer to the S vacancy [46,47]. The recombination rate of photogenerated electron-hole pairs was evaluated by transient photocurrent response (Fig. S16). The highest instantaneous photocurrent density of Vs-1T$_{0.15}$-WCS demonstrated the presence of S vacancies accelerated the carrier migration efficiency on Vs-1T$_{0.15}$-WCS. And the smallest impedance arc radius of Vs-1T-WS$_2$ verified its inherent metallicity, which facilitated the rapid migration of photogenerated carriers on CdS to Vs-1T-WS$_2$ (Fig. 3c). In addition, Vs-1T$_{0.15}$-WCS had instantaneous photocurrent response at different wavelengths, which demonstrated the wide range of optical absorption properties. Kelvin probe force microscopy (KPFM) was characterized to analyze the charge transfer mechanism at the interface (Fig. 3d–f). In the AFM image, the catalyst in the middle position (green dashed box) was regarded as the CdS (labeled as B), while the edge position with a height of 5 µm (red dashed box) was regarded as Vs-1T-WS$_2$ (labeled as A). By comparing the surface photovoltage images of Vs-1T$_{0.15}$-WCS in the dark and under light irradiation at wavelengths λ > 420 nm, the potential at position A decreased ~160 mV after light irradiation, while the potential at position B increased ~70 mV, which implied the transfer of electrons from CdS to
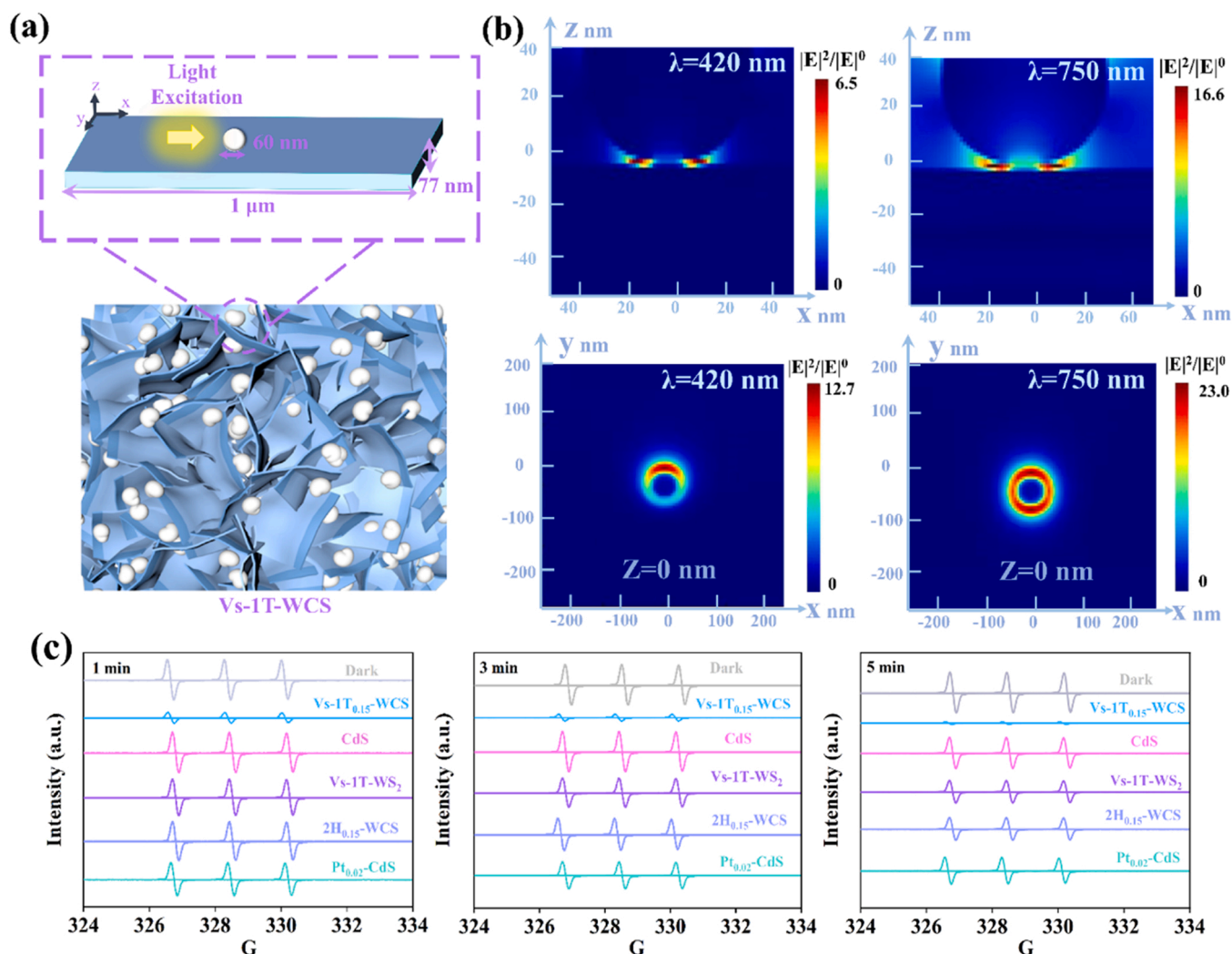
Fig. 5. The promotion of photothermal effect on the carries transmission. (a) Simplified model of Vs-1T-WCS for FDTD simulation, (b) FDTD simulated local field intensity variations at 420 nm and 750 nm, (c) ESR spectra of the prepared samples at different time ranges (TEMPO-e$^-$).

Vs-1T-WS$_2$. This directed electron migration path reduced the photo-generated electron-hole complexation rate and the abundant S vacancies on Vs-1T-WS$_2$ acted as electron collectors to promote the photocatalytic performance.

3.4. Photocatalytic mechanism

The modulation of the electronic structure by S vacancies and the charge transfer paths at the interface were further elaborated on the density functional theory (DFT) calculations. The work functions (Φ) of Vs-1T-WS$_2$ (4.28 eV) and CdS (6.06 eV) were calculated to determine the corresponding Fermi energy levels (E_f), respectively. When Vs-1T-WS$_2$ and CdS contacted each other to form a tight heterogeneous interface, free electrons flowed spontaneously from Vs-1T-WS$_2$ at the high Fermi energy level to CdS at the low Fermi energy level (Fig. 4a and b) [48,49]. Both the total density states of Vs-1T-WS$_2$ and 1T-WS$_2$ crossed the E_f, which demonstrated their potential to induce photothermal effects as metal co-catalysts (Fig. 4c). As observed, the density of states near the Fermi level of Vs-1T-WS$_2$ was significantly increased compared to the pristine 1T-WS$_2$ due to the local lattice distortion around the S vacancies. The calculated charge density difference between Vs-1T-WS$_2$ and CdS further confirmed the above conclusion (Fig. 4d). Due to the intimate contacted between Vs-1T-WS$_2$ and CdS, electrons were depleted on the side close to Vs-1T-WS$_2$, while electron

enrichment occurred on the CdS side at the interface. This result illustrated the tendency of electron enrichment on CdS in the dark, which was consistent with the result of KPFM and XPS. Calculating the hydrogen adsorption Gibbs free energy (ΔG_H) of the catalyst to demonstrate the adsorption capacity of *H was an effective method to verify the photocatalytic performance from a theoretical view (Fig. 4e). By comparing the ΔG_H on unsaturated S sites and S vacancies, it was clearly obtained that the *H was more readily adsorbed on the S vacancies of Vs-1T-WS$_2$. This was due to the introduction of S vacancies which significantly reduced the ΔG_H of Vs-1T-WS$_2$ (0.85 eV). Moreover, the ΔG_H of Vs-1T$_{0.15}$-WCS was significantly lower than that of CdS (2.27 eV), which indicated that Vs-1T$_{0.15}$-WCS crossed a lower energy barrier to facilitate the photocatalytic hydrogen evolution. In summary, the difference in catalyst activity arose from the acceleration of interfacial electron migration by photothermal effects and the ability to adsorb *H and trap electrons on S vacancies.

In order to illustrate the promotion of photothermal effect on the carries transmission in the built-in electric field of Vs-1T-WS$_2$ and CdS [50], FDTD theoretical simulation was carried out to detect the trend of the local electromagnetic field intensity ($|E|^2/|E|^0$) of Vs-1T-WCS under different wavelengths of monochromatic light irradiation (420 nm and 750 nm) (Fig. 5a and b). The results indicated that the magnetic field enhancement effect was caused by the presence of the built-in electric field at the interface and the interfacial electron enrichment effect due to
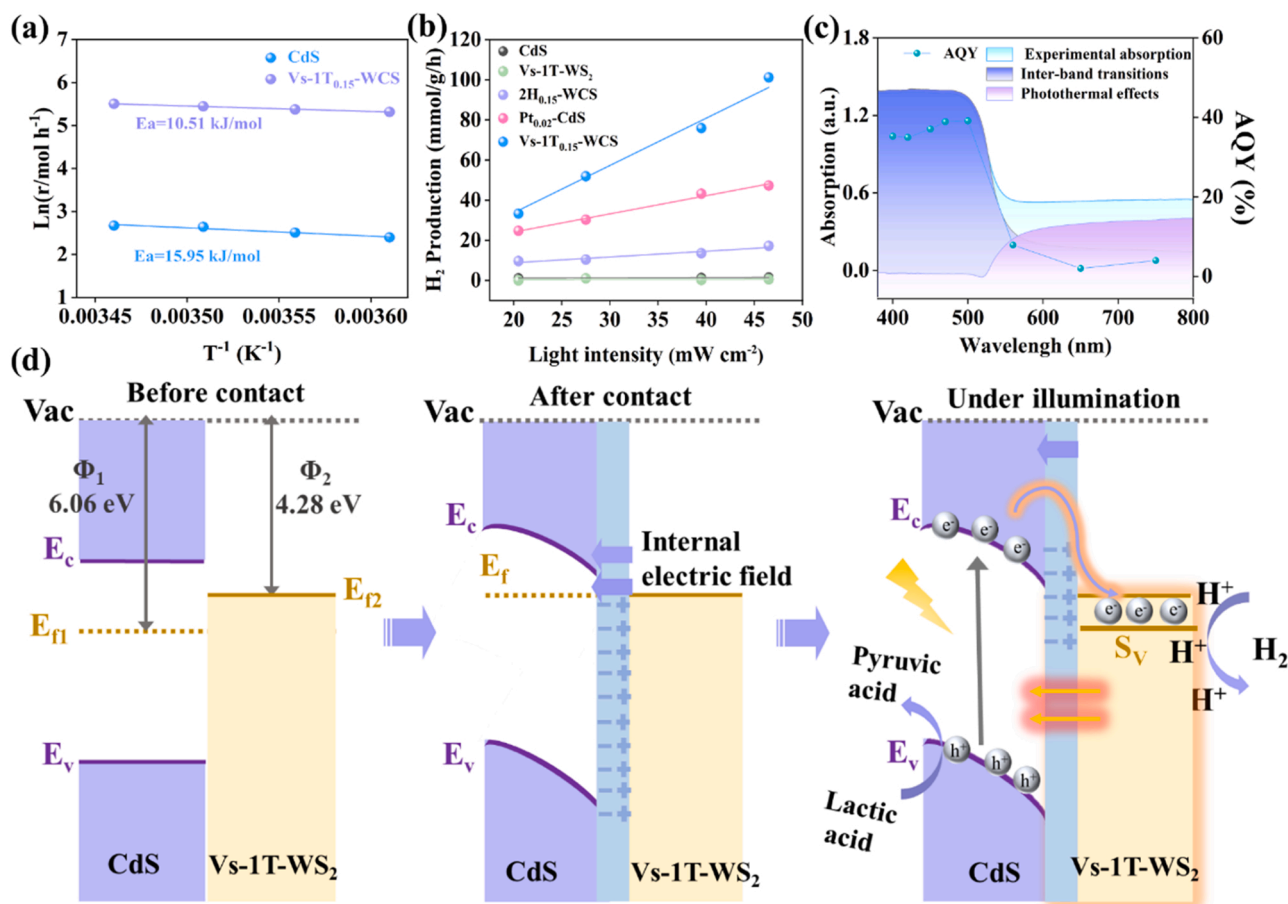
Fig. 6. Photocatalytic mechanism. (a) Apparent activation energy of the reaction system at different temperatures, (b) linear relationship between photocatalytic hydrogen evolution rate and light intensity, (c) contribution composition at different wavelengths regarding the photothermal effect induced by Vs-1T-WS₂ and inter band migration of carriers in Vs-1T-WCS, (c) Schematic diagram of the energy band structure and photocatalytic hydrogen precipitation of Vs-1T-WCS.

the photothermal effect induced by Vs-1T-WS$_2$. Meanwhile, the electromagnetic field intensity was strongly influenced by the incident light wavelength. Under light excitation at 750 nm, the electromagnetic field intensity at the interface was significantly enhanced compared to under light excitation at 420 nm. Since the enhanced electromagnetic field strength favored the transport of photogenerated carriers from CdS to Vs-1T-WS$_2$ [51,52], the contribution of the photothermal effect induced by metallic co-catalysts was further clarified. The variation of the captured photogenerated electron concentration with time in the dark and in the light was recorded in the ESR spectra (Fig. 5c). The ESR signal intensity of Vs-1T$_{0.15}$-WCS diminished fastest with increasing light irradiation time, which implied that more photogenerated electrons were trapped due to the synergistic effect of photothermal effects and efficient interfacial electron migration [53,54].

To explore the influence of Vs-1T-WS$_2$-induced photothermal effects on the reaction kinetics in the photoreaction system, the temperature-dependent kinetic experiments for the photocatalytic hydrogen evolution were carried out accordingly. The photocatalytic hydrogen evolution rate of the prepared catalysts exhibited a linear dependence on the reaction temperature (277–289 K) (Fig. 6a). Notably, the *Ea* of Vs-1T$_{0.15}$-WCS decreased significantly to 10.51 kJ/mol compared with that of pristine CdS (15.96 kJ/mol), indicating that the photothermal induced by Vs-1T-WS$_2$ significantly accelerated the reaction kinetics to promote photocatalytic hydrogen evolution. In further, the photocatalytic hydrogen evolution rate was found to exhibit a regular linear relationship with increasing light intensity (Fig. 6b), which confirmed the more photogenerated carriers were migrated to S vacancies effectively with the light flux increasing. Meanwhile, the increase of reaction

level obtained in Vs-1T-WCS indicated that the additional energy other than light energy was injected to accelerate the migration of photogenerated carriers at the interface. The inter band transition of photocarriers was found to be the main driving force for the photocatalytic hydrogen evolution based on the wavelength match of AQY and carrier inter band transition contributions (Fig. 6c) [55].

Based on the above analysis, we proposed a feasible mechanism for the Vs-1T-WCS enhanced photocatalytic hydrogen evolution (Fig. 6d). Due to the difference in E_f, the contact between CdS and Vs-1T-WS$_2$ leaded to a charge redistribution with the CdS side in the negatively charged and Vs-1T-WS$_2$ in the positively charged. This charge distribution resulted in a downward bending of the energy band near the CdS side that formed a built-in electric field from Vs-1T-WS$_2$ toward CdS. An ohmic contact was formed at the heterogeneous interface to achieve the directional migration of carriers. Under visible light irradiation, the photogenerated electrons and holes in CdS were separated. Driven by the built-in electric field, the photogenerated electrons transferred to the CB of CdS were rapidly guided out and migrated directionally to the S vacancies in Vs-1T-WS$_2$. The S vacancies both acted as adsorption sites for *H and capture sites for photogenerated electrons, which could promptly reduce the adsorbed *H to H$_2$. Notably, the time scale of lattice heating induced by hot carrier relaxation was in the range of 1–10 ps, which was much lower than the time scale of local electrolyte temperature increase induced by heat dissipation (100 ps-10 ns). Therefore, the reduction of apparent activation energy was due to the photothermal effect that accelerated the reaction kinetics in the system. More importantly, the photothermal effect accelerated the targeted migration of more electrons from CdS to the S vacancies that acted as both adsorption

and activation sites, while the holes on the VB of CdS were trapped by lactic acid.

4. Conclusions

In conclusion, S vacancies with a dual function was constructed at Vs-1T-WCS, and the ultrafast migration of carriers from CdS to Vs-1T-WS$_2$ was achieved through the synergistic effect of electron modulation and photothermal effect at the interface. Here, the rationally designed S vacancies provided a platform for the directional migration of photo-generated electrons, and the introduction of Vs-1T-WS$_2$ was able to act as both an electron trap to collect more electrons for hydrogen proton reduction and induced a photothermal effect to increase the carrier migration rate. The photocatalytic hydrogen evolution efficiency of Vs-1T$_{0.15}$-WCS under visible light irradiation was 70.9 mmol/g/h, and the AQY at 500 nm was 39.1%, which was 47 times higher than that of pristine CdS. This work not only provided the possibility for CdS-based photocatalysts to achieve ultra-high performance hydrogen evolution, but also created an opportunity for non-precious metal co-catalysts for photothermal-assisted photocatalytic hydrogen evolution.

CRediT authorship contribution statement

Yuan Tang: performed the experiments, data analysis and wrote the manuscript. **Tao Yu:** established the research line and supervised the current work. **Xin Tan:** co-supervised the current work. **Wei Zhou**, **Qianqian Shang:** theoretical calculations. **Lequan Liu**, **Huaiyuan Wang**, and **Jinhua Ye:** resources. **Huilin Hu**, **Yuchen Guo**, and **Zhiqiang Li**, **Yizhong Zhang** were involved in the analysis of data and revised the manuscript. All the authors reviewed, approved, and contributed to the final version of the manuscript.

Declaration of Competing Interest

The authors declare that they have no known competing financial interests or personal relationships that could have appeared to influence the work reported in this paper.

Appendix A. Supporting information

Supplementary data associated with this article can be found in the online version at doi:10.1016/j.apcatb.2022.121295.

References

[1] X.H. Wang, X.H. Wang, J.F. Huang, S.X. Li, A. Meng, Z.J. Li, Interfacial chemical bond and internal electric field modulated Z-scheme S-v-ZnIn$_2$S$_4$/MoSe$_2$ photocatalyst for efficient hydrogen evolution, Nat. Commun. 12 (2021) 11.
[2] Y. Zhao, C. Ding, J. Zhu, W. Qin, X. Tao, F. Fan, R. Li, C. Li, A hydrogen farm strategy for scalable solar hydrogen production with particulate photocatalysts, Angew. Chem. Int. Ed. 59 (2020) 9653–9658.
[3] B.Y. Dai, J.J. Fang, Y.R. Yu, M.L. Sun, H.M. Huang, C.H. Lu, J.H. Kou, Y.J. Zhao, Z. Z. Xu, Construction of infrared-light-responsive photoinduced carriers driver for enhanced photocatalytic hydrogen evolution, Adv. Mater. 32 (2020) 9.
[4] W. Bi, X. Li, L. Zhang, T. Jin, L. Zhang, Q. Zhang, Y. Luo, C. Wu, Y. Xie, Molecular co-catalyst accelerating hole transfer for enhanced photocatalytic H$_2$ evolution, Nat. Commun. 6 (2015) 8647.
[5] D. Gao, J. Xu, L. Wang, B. Zhu, H. Yu, J. Yu, Optimizing atomic hydrogen desorption of sulfur-rich NiS$_{1+x}$ cocatalyst for boosting photocatalytic H$_2$ evolution, Adv. Mater. 34 (2022), 2108475.
[6] J.Y. Zhang, S. Yuan, J. Lin, Cd$_{1-x}$Zn$_x$S nanorod solid solutions with sulfur vacancies as effective electron traps for highly efficient photocatalytic hydrogen evolution, J. Phys. Chem. C 125 (2021) 25600–25607.
[7] K. Yu, H.B. Huang, X.Y. Zeng, J.Y. Xu, X.T. Yu, H.X. Liu, H.L. Cao, J. Lu, R. Cao, CdZnS nanorods with rich sulphur vacancies for highly efficient photocatalytic hydrogen production, Chem. Commun. 56 (2020) 7765–7768.
[8] J.L. Yang, Y.L. He, H. Ren, H.L. Zhong, J.S. Lin, W.M. Yang, M.D. Li, Z.L. Yang, H. Zhang, Z.Q. Tian, J.F. Li, Boosting photocatalytic hydrogen evolution reaction using dual plasmonic antennas, ACS Catal. 11 (2021) 5047–5053.
[9] Y. Shi, J. Li, C. Mao, S. Liu, X. Wang, X. Liu, S. Zhao, X. Liu, Y. Huang, L. Zhang, Van Der Waals gap-rich BiOCl atomic layers realizing efficient, pure-water CO$_2$-to-CO photocatalysis, Nat. Commun. 12 (2021) 5923.
[10] Y.-Q. Zhou, L. Zhang, H.-L. Suo, W. Hua, S. Indris, Y. Lei, W.-H. Lai, Y.-X. Wang, Z. Hu, H.-K. Liu, S.-L. Chou, S.-X. Dou, Atomic cobalt vacancy-cluster enabling optimized electronic structure for efficient water splitting, Adv. Funct. Mater. 31 (2021), 2101797.
[11] J. Zhao, S. Xue, R. Ji, B. Li, J. Li, Localized surface plasmon resonance for enhanced electrocatalysis, Chem. Soc. Rev.. 50 (2021) 12070–12097.
[12] S. Mukherjee, F. Libisch, N. Large, O. Neumann, L.V. Brown, J. Cheng, J.B. Lassiter, E.A. Carter, P. Nordlander, N.J. Halas, Hot electrons do the impossible: plasmon-induced dissociation of H-2 on Au, Nano Lett. 13 (2013) 240–247.
[13] D. Devasia, A.J. Wilson, J. Heo, V. Mohan, P.K. Jain, A rich catalog of C-C bonded species formed in CO$_2$ reduction on a plasmonic photocatalyst, Nat. Commun. 12 (2021) 2612.
[14] G. Kumari, X. Zhang, D. Devasia, J. Heo, P.K. Jain, Watching visible light-driven CO$_2$ reduction on a plasmonic nanoparticle catalyst, Acs Nano 12 (2018) 8330–8340.
[15] N. Hogan, S. Wu, M. Sheldon, Photothermalization and hot electron dynamics in the steady state, J. Phys. Chem. C 124 (2020) 4931–4945.
[16] S. Shi, Z. Sun, Y.H. Hu, Synthesis, stabilization and applications of 2-dimensional 1T metallic MoS$_2$, J. Mater. Chem. A 6 (2018) 23932–23977.
[17] J.T. Robinson, S.M. Tabakman, Y. Liang, H. Wang, H.S. Casalongue, V. Daniel, H. Dai, Ultrasmall reduced graphene oxide with high near-infrared absorbance for photothermal therapy, J. Am. Chem. Soc. 133 (2011) 6825–6831.
[18] Z. Wei, C. Hsu, H. Almakrami, G. Lin, J. Hu, X. Jin, E. Agar, F. Liu, Ultra-high-aspect-ratio vertically aligned 2D MoS$_2$-1D TiO$_2$ nanobelt heterostructured forests for enhanced photoelectrochemical performance, Electrochim. Acta 316 (2019) 173–180.
[19] Z. Li, W. Zhou, Y. Tang, X. Tan, Y. Zhang, Z. Geng, Y. Guo, L. Liu, T. Yu, J. Ye, Insights into the operation of noble-metal-free cocatalyst 1T-WS$_2$-decorated Zn$_{0.5}$Cd$_{0.5}$S for enhanced photocatalytic hydrogen evolution, ChemSusChem 14 (2021) 4752–4763.
[20] Z. Liang, S. Yang, X. Wang, H. Cui, X. Wang, J. Tian, The metallic 1T-phase WS$_2$ nanosheets as cocatalysts for enhancing the photocatalytic hydrogen evolution of g-C$_3$N$_4$ nanotubes, Appl. Catal. B-Environ. 274 (2020), 119114.
[21] S.S. Chou, B. Kaehr, J. Kim, B.M. Foley, M. De, P.E. Hopkins, J. Huang, C. J. Brinker, V.P. Dravid, Chemically exfoliated MoS$_2$ as near-infrared photothermal agents, Angew. Chem. Int. Ed. 52 (2013) 4160–4164.
[22] Y. Zhang, Y. Zhang, H. Zhang, L. Bai, L. Hao, T. Ma, H. Huang, Defect engineering in metal sulfides for energy conversion and storage, Coord. Chem. Rev. 448 (2021), 214147.
[23] Y. Cui, X. Guo, J. Zhang, Xa Li, X. Zhu, W. Huang, Di-defects synergy boost electrocatalysis hydrogen evolution over two-dimensional heterojunctions, Nano Res. 15 (2022) 677–684.
[24] J. Gao, F. Zhang, H. Xue, L. Zhang, Y. Peng, X. Li, Y. Gao, N. Li, L. Ge, In-situ synthesis of novel ternary CdS/PdAg/g-C$_3$N$_4$ hybrid photocatalyst with significantly enhanced hydrogen production activity and catalytic mechanism exploration, Appl. Catal. B-Environ. 281 (2021), 119509.
[25] D. Ren, R. Shen, Z. Jiang, X. Lu, X. Li, Highly efficient visible-light photocatalytic H-2 evolution over ^{2}D–^{2}D CdS/Cu7S4 layered heterojunctions, Chin. J. Catal. 41 (2020) 31–40.
[26] A. Han, X. Zhou, X. Wang, S. Liu, Q. Xiong, Q. Zhang, L. Gu, Z. Zhuang, W. Zhang, F. Li, D. Wang, L.-J. Li, Y. Li, One-step synthesis of single-site vanadium substitution in 1T-WS$_2$ monolayers for enhanced hydrogen evolution catalysis, Nat. Commun. 12 (2021) 709.
[27] Z. Lai, Q. He, T.Thu Ha, D.V.M. Repaka, D.-D. Zhou, Y. Sun, S. Xi, Y. Li, A. Chaturvedi, C. Tan, B. Chen, G.-H. Nam, B. Chen, C. Ling, W. Zhai, S. Hu, D. Hu, V. Sharma, Z. Hu, Y. Chen, Z. Zhang, Y. Yu, X.R. Wang, R.V. Ramanujan, Y. Ma, K. Hippalgaonkar, H. Zhang, Metastable 1T '-phase group VIB transition metal dichalcogenide crystals, Nat. Mater. 20 (2021) 1113–1120, 1113-+.
[28] W. Ding, L. Hu, J. Dai, X. Tang, R. Wei, Z. Sheng, C. Liang, D. Shao, W. Song, Q. Liu, M. Chen, X. Zhu, S. Chou, X. Zhu, Q. Chen, Y. Sun, S.X. Dou, Highly ambient-stable 1T-MoS$_2$ and 1T-WS$_2$ by hydrothermal synthesis under high magnetic fields, Acs Nano 13 (2019) 1694–1702.
[29] D. Xu, P. Xu, Y. Zhu, W. Peng, Y. Li, G. Zhang, F. Zhang, T.E. Mallouk, X. Fan, High yield exfoliation of WS$_2$ crystals into 1-2 Layer semiconducting nanosheets and efficient photocatalytic hydrogen evolution from WS$_2$/CdS nanorod composites, Acs Appl. Mater. Interface. 10 (2018) 2810–2818.
[30] J. Zhang, Y. Song, X. Dong, H. Jiang, J. Tang, H. Li, Umbrella-like CdS single crystal: exposed (002) facets and enhanced photocatalytic properties, J. Mater. Sci. 55 (2020) 11167–11176.
[31] X. Zhang, Z. Chen, Y. Luo, X. Han, Q. Jiang, T. Zhou, H. Yang, J. Hu, Construction of NH2-MIL-125(Ti)/CdS Z-scheme heterojunction for efficient photocatalytic H$_2$ evolution, J. Hazard. Mater. 405 (2021), 124128.
[32] X. Wang, Y. Zhang, H. Si, Q. Zhang, J. Wu, L. Gao, X. Wei, Y. Sun, Q. Liao, Z. Zhang, K. Ammarah, L. Gu, Z. Kang, Y. Zhang, Single-atom vacancy defect to trigger high-efficiency hydrogen evolution of MoS$_2$, J. Am. Chem. Soc. 142 (2020) 4298–4308.

[33] C. Du, Q. Zhang, Z. Lin, B. Yan, C. Xia, G. Yang, Half-unit-cell $ZnIn_2S_4$ monolayer with sulfur vacancies for photocatalytic hydrogen evolution, Appl. Catal. B-Environ. 248 (2019) 193–201.

[34] Q. Xu, Y. Liu, H. Jiang, Y. Hu, H. Liu, C. Li, Unsaturated sulfur edge engineering of strongly coupled MoS_2 nanosheet-carbon macroporous hybrid catalyst for enhanced hydrogen generation, Adv. Energy Mater. 9 (2019), 1802553.

[35] K. Zhang, Y. Dai, Z. Zhou, S.U. Jan, L. Guo, J.R. Gong, Polarization-induced saw-tooth-like potential distribution in zincblende-wurtzite superlattice for efficient charge separation, Nano Energy 41 (2017) 101–108.

[36] Y. Deng, L.R.L. Ting, P.H.L. Neo, Y.-J. Zhang, A.A. Peterson, B.S. Yeo, Operando Raman spectroscopy of amorphous molybdenum sulfide (MoS_x) during the electrochemical hydrogen evolution reaction: identification of sulfur atoms as catalytically active sites for H^+ reduction, ACS Catal. 6 (2016) 7790–7798.

[37] A. Meng, X. Yuan, T. Shen, J. Zhao, G. Song, Y. Lin, Z. Li, Amorphous nickel sulfide nanoparticles anchored on N-doped graphene nanotubes with superior properties for high-performance supercapacitors and efficient oxygen evolution reaction, Nanoscale 12 (2020) 4655–4666.

[38] Z. Zhang, Y. Dong, H. Sun, G. Liu, S. Liu, X. Yang, Defect-rich 2D reticulated MoS_2 monolayers: facile hydrothermal preparation and marvellous photoelectric properties, J. Taiwan Inst. Chem. Eng. 101 (2019) 221–230.

[39] B. Mahler, V. Hoepfner, K. Liao, G.A. Ozin, Colloidal synthesis of $1T-WS_2$ and $2H$-WS_2 nanosheets: applications for photocatalytic hydrogen evolution, J. Am. Chem. Soc. 136 (2014) 14121–14127.

[40] D. Voiry, H. Yamaguchi, J. Li, R. Silva, D.C.B. Alves, T. Fujita, M. Chen, T. Asefa, V. B. Shenoy, G. Eda, M. Chhowalla, Enhanced catalytic activity in strained chemically exfoliated WS_2 nanosheets for hydrogen evolution, Nat. Mater. 12 (2013) 850–855.

[41] S. Song, J. Qu, P. Han, M.J. Hulsey, G. Zhang, Y. Wang, S. Wang, D. Chen, J. Lu, N. Yan, Visible-light-driven amino acids production from biomass-based feedstocks over ultrathin CdS nanosheets, Nat. Commun. 11 (2020) 4899.

[42] Z. Zhang, X. Xia, W. Yang, L. Wang, Y. Liu, Photothermal effect and continuous hot electrons injection synergistically induced enhanced molecular oxygen activation for efficient selective oxidation of benzyl alcohol over plasmonic $W_{18}O_{49}/ZnIn_2S_4$ photocatalyst, Appl. Catal. B-Environ. 299 (2021), 120675.

[43] Z. Zhang, J. Huang, Y. Fang, M. Zhang, K. Liu, B. Dong, A nonmetal plasmonic Z-scheme photocatalyst with UV- to NIR-driven photocatalytic protons reduction, Adv. Mater. 29 (2017), 1606688.

[44] Y. Qi, J. Jiang, X. Liang, S. Ouyang, W. Mi, S. Ning, L. Zhao, J. Ye, Fabrication of black In_2O_3 with dense oxygen vacancy through dual functional carbon doping for enhancing photothermal CO_2 hydrogenation, Adv. Funct. Mater. 31 (2021), 2100908.

[45] C.-C. Shen, Y.-N. Liu, X. Zhou, H.-L. Guo, Z.-W. Zhao, K. Liang, A.-W. Xu, Large improvement of visible-light photocatalytic H_2 evolution based on cocatalyst-free $Zn_{0.5}Cd_{0.5}S$ synthesized through a two-step process, Catal. Sci. Technol. 7 (2017) 961–967.

[46] S.K. Cushing, J. Li, F. Meng, T.R. Senty, S. Suri, M. Zhi, M. Li, A.D. Bristow, N. Wu, Photocatalytic activity enhanced by plasmonic resonant energy transfer from metal to semiconductor, J. Am. Chem. Soc. 134 (2012) 15033–15041.

[47] X. Lu, C.Y. Toe, F. Ji, W. Chen, X. Wen, R.J. Wong, J. Seidel, J. Scott, J.N. Hart, Y. H. Ng, Light-induced formation of MoO_xS_y Clusters on CdS nanorods as cocatalyst for enhanced hydrogen evolution, Acs Appl. Mater. Interfaces 12 (2020) 8324–8332.

[48] M. Tang, Y. Ao, C. Wang, P. Wang, Rationally constructing of a novel dual Z-scheme composite photocatalyst with significantly enhanced performance for neonicotinoid degradation under visible light irradiation, Appl. Catal. B-Environ. 270 (2020), 118918.

[49] P. Wen, Y. Sun, H. Li, Z. Liang, H. Wu, J. Zhang, H. Zeng, S.M. Geyer, L. Jiang, A highly active three-dimensional Z-scheme $ZnO/Au/g-C_3N_4$ photocathode for efficient photoelectrochemical water splitting, Appl. Catal. B-Environ. 263 (2020), 118180.

[50] X. Li, H. Jiang, C. Ma, Z. Zhu, X. Song, H. Wang, P. Huo, X. Li, Local surface plasma resonance effect enhanced Z-scheme $ZnO/Au/g-C_3N_4$ film photocatalyst for reduction of CO_2 to CO, Appl. Catal. B-Environ. 283 (2021), 119638.

[51] S. Wang, X. Wang, Photocatalytic CO_2 reduction by CdS promoted with a zeolitic imidazolate framework, Appl. Catal. B-Environ. 162 (2015) 494–500.

[52] Q. Yu, P. Gao, K.Y. Zhang, X. Tong, H. Yang, S. Liu, J. Du, Q. Zhao, W. Huang, Luminescent gold nanocluster-based sensing platform for accurate H_2S detection in vitro and in vivo with improved anti-interference, Light-Sci. Appl. 6 (2017) 17107.

[53] H. Hao, J.-L. Shi, H. Xu, X. Li, X. Lang, N-hydroxyphthalimide-TiO_2 complex visible light photocatalysis, Appl. Catal. B-Environ. 246 (2019) 149–155.

[54] X. Li, H. Xu, J.-L. Shi, H. Hao, H. Yuan, X. Lang, Salicylic acid complexed with TiO_2 for visible light-driven selective oxidation of amines into imines with air, Appl. Catal. B-Environ. 244 (2019) 758–766.

[55] L. Liu, P. Li, B. Adisak, S. Ouyang, N. Umezawa, J. Ye, R. Kodiyath, T. Tanabe, G. V. Ramesh, S. Ueda, H. Abe, Gold photosensitized $SrTiO_3$ for visible-light water oxidation induced by Au interband transitions, J. Mater. Chem. A 2 (2014) 9875–9882.